Research Square

Preprints are preliminary reports that have not undergone peer review.
They should not be considered conclusive, used to inform clinical practice,
or referenced by the media as validated information.

First-passage fracture probability in stochastic phase-field models

Zhichao Zhang
Yangzhou University
Peifeng Gao
gaopf@lzu.edu.cn
Ministry of Education, Lanzhou University
Chaofan Du
Yangzhou University

Research Article

Keywords: phase-field fracture, first passage, Fokker–Planck equation, reflected Langevin dynamics, survival probability

Posted Date: November 10th, 2026

DOI: https://doi.org/10.21203/rs.3.rs-11418494/v1

License: This work is licensed under a Creative Commons Attribution 4.0 International License.
Read Full License

Additional Declarations: No competing interests reported.

First-passage fracture probability in stochastic phase-field models

Zhichao Zhang[1], Peifeng Gao[2,3*], Chaofan Du[1]

[1] College of Civil Engineering and Transportation, Yangzhou University, Yangzhou 225000, China

[2] Key Laboratory of Mechanics on Western Disaster and Environment, Ministry of Education; and College of Civil Engineering and Mechanics, Lanzhou University, Lanzhou 730000, China

[3] Key Laboratory of Special Functional Materials and Devices, Ministry of Education, Lanzhou University, Lanzhou 730000, China

*Corresponding author: gaopf@lzu.edu.cn

Abstract

Predicting fracture probability from an evolving damage field requires an explicit event definition. In the underlying probability space, we define fracture as the set of realizations whose damage trajectories first reach a critical surface by a given time, establishing a first-passage theory within a finite-element stochastic AT2 phase-field model. Mesoscopic fluctuations follow a reflected Langevin process: reflecting boundaries enforce admissible damage bounds, while an absorbing boundary imparts event irreversibility. The corresponding Fokker–Planck equation establishes a mass–flux closure where lost survival mass gives cumulative fracture probability, outward absorption flux gives its evolution rate, and the flux-to-survival ratio defines the effective hazard rate. Conditioning and averaging over exogenous material, geometric, and loading uncertainties yield a survival-weighted population hazard. Seven numerical cases verify probability conservation, delineate quasi-stationary and Kramers regimes, demonstrate one- and two-dimensional mechanical coupling, and jointly calibrate mobility and noise intensity from first-passage and intact-state relaxation data. In a loading–unloading example, cumulative fracture probability remains at 0.3809 despite a nearly zero post-unloading tail probability. This framework unifies fracture as a load-driven probability evolution, intrinsically linking spatial damage dynamics to path-dependent fracture probability.

Keywords: phase-field fracture; first passage; Fokker–Planck equation; reflected Langevin dynamics; survival probability

1 Introduction

Material fracture in solid mechanics has long been investigated primarily within a deterministic framework. Whether through classical continuum fracture mechanics or computational approaches developed over recent decades—such as variational phase-field fracture models and the extended finite element method—the underlying description characterizes failure as an inevitable outcome once the applied load reaches a critical material limit. Yet viewing the same physical process from an alternative perspective yields an instructive picture: the entire fracture process can be regarded as a probability evolution in the underlying probability space driven by the applied load. Under low loading, probability mass remains concentrated near the intact state; as the load increases, this probability mass undergoes directed drift and diffusive transport toward a critical state, causing the fracture probability to accumulate; macroscopic "deterministic" failure then corresponds to the regime in which substantial probability mass crosses the critical boundary and the cumulative fracture probability approaches unity. From this viewpoint, the central question of fracture mechanics shifts from whether a material fractures at a given load to how its fracture probability evolves in probability space over a loading history. The present work follows this probability-evolution perspective to formulate and compute fracture behavior.

Viewed from this perspective, the statistical approach to fracture was the first to address fracture probability directly. Since Weibull (1951) introduced extreme-value distributions to represent fracture strength, statistical fracture mechanics has typically proceeded by calibrating distribution parameters from experiments and evaluating failure probability at a prescribed stress level (Freudenthal 1968). Although Weibull formulations remain widely used to characterize strength scatter in brittle materials, their scale and shape parameters are usually calibrated phenomenologically from data rather than derived from microstructural evolution. Bažant and Pang (2007) combined activation-energy arguments with extreme-value statistics to derive strength distributions and size effects from atomic bond-breakage rates, thereby linking statistical fracture to rate processes, yet without resolving spatial damage trajectories or first-passage dynamics. Time-dependent Weibull models, competing-risk models, and empirical hazard formulations further incorporate temporal dependence, but extending them to general dynamic loading histories, multiaxial stress states, and complex geometries still requires additional modeling or calibration. Along the main thread of the present study, the common feature of these approaches is that fracture probability arises from fitting and assigning distributions to experimental data rather than emerging from damage dynamics in probability space—probability is treated as a calibrated static quantity rather than a dynamical variable that evolves continuously along a loading path.

A second, and the most widely adopted, route in engineering is the deterministic computational approach. Francfort and Marigo (1998) reformulated brittle fracture as an energy-minimization problem, and Bourdin et al. (2000) approximated sharp-crack functionals via elliptic phase-field regularization. Miehe et al. (2010a, b) subsequently developed tension–compression splits and thermodynamically consistent phase-field formulations; comprehensive reviews are available in Bourdin et al. (2008), Ambati et al. (2015) and Wu et al. (2020), and dynamic fracture has also been addressed using phase-field models (Karma et al. 2001). In the AT2 regularization (Ambrosio and Tortorelli 1990), material damage is represented by a continuous scalar phase field whose gradient-flow evolution couples quasi-static mechanical equilibrium to the damage variable. Such formulations characterize a single deterministic trajectory in state space: given a loading history, the phase field evolves along a unique path until failure. In engineering practice, however, structural fracture rarely occurs repeatedly at the exact same load or location; because when and where a structure fractures are

influenced by multiple random factors, the primary quantity of interest is often the failure probability at a given loading level. A common computational practice is therefore to inspect the distribution at a single observation time and declare fracture whenever the phase-field variable or its driving force exceeds a critical threshold. While convenient, this snapshot-exceedance criterion attaches probability to an instantaneous state inspection, discarding both the prior loading history and the first-passage nature of the fracture event. Consequently, fracture probability still does not appear as a quantity evolving continuously in probability space over the loading history, but remains an a posteriori diagnostic of deterministic trajectories.

Formulating fracture probability genuinely as an evolving quantity in probability space requires a mathematical theory that governs the continuous-time evolution of probability density—a complementary foundation provided by statistical physics and stochastic process theory. Langevin (1908) introduced the stochastic force description of Brownian fluctuations, and Chandrasekhar (1943) systematized stochastic problems in physics and astronomy. Within this framework, the Fokker–Planck (FP) equation governs the continuous-time evolution of probability density in state space (Risken 1989; Gardiner 2004; van Kampen 2007), directly answering the core question of how probability mass drifts, diffuses, and redistributes. Kramers (1940) derived the classical escape rate of a Brownian particle over a potential barrier, with subsequent developments reviewed by Hänggi et al. (1990), rigorous mathematical treatments established via large-deviation and metastability theories (Freidlin and Wentzell 2012; Bovier et al. 2005), and domains of validity analyzed by Berglund (2013), building on Eyring's transition-state theory (Eyring 1935). Furthermore, the fluctuation–dissipation relations established by Callen and Welton (1951) and Kubo (1966) provide a closure basis for matching fluctuation intensity to dissipation mechanisms; first-passage time statistics are classical (Redner 2001); and the long-time behavior of surviving sample paths under absorbing boundary conditions is characterized by the quasi-stationary distribution (QSD) (Méléard and Villemonais 2012; Collet et al. 2013; Benaim et al. 2021). Together, these theories support a path-based description of failure: failure corresponds to the event in which a stochastic trajectory first reaches a designated boundary, and its probability is generated intrinsically by the evolution equation itself rather than by an instantaneous state inspection or an externally assigned distribution. This provides the exact mathematical toolkit needed to realize the probability-evolution perspective.

Engineering uncertainty quantification likewise provides mature structural reliability tools (Rackwitz 2001). The probability density evolution method (PDEM) and generalized density evolution equation (GDEE) developed by Li and Chen (2006, 2008) offer an effective route for stochastic structural response and dynamic reliability analysis, as systematically expounded in Li and Chen (2009) (see also Zhang and Lv 2010), while rare-event techniques such as subset simulation substantially reduce the cost of estimating small failure probabilities in high dimensions (Au and Beck 2001). With regard to probability evolution, these methods do evolve probability densities, but the propagated object is primarily the density of uncertain inputs or structural responses: randomness originates from external system parameters, whereas the conditional dynamical system itself remains deterministic. Although probability density evolution methods can accommodate multiple random factors, their description of fracture does not depart fundamentally from the deterministic solid-mechanics paradigm: once the exogenous random factors are conditioned upon, the problem reduces to a deterministic fracture analysis in which failure is judged along each individual deterministic trajectory, and the resulting failure probability is an outer statistical aggregation after trajectory-wise inspection rather than an intrinsic evolution of the fracture event itself in probability space.

Synthesizing the above review, the missing link is clear: a formulation is needed in which fracture probability is generated continuously by the damage dynamics itself as an evolving quantity

in probability space while preserving the first-passage character of the fracture event. To this end, we define the critical damage surface as an absorbing boundary of the intact state domain and identify fracture with the first arrival of a stochastic damage trajectory at this surface. Once unresolved mesoscopic dynamics are represented by effective noise, the first-passage time becomes a random variable whose cumulative distribution defines the cumulative fracture probability. Generated jointly by stochastic phase-field dynamics, boundary absorption, and probability mass conservation rather than instantaneous threshold exceedance, this quantity precisely realizes the physical picture envisioned at the outset: the loading history drives the evolution of probability density within the intact domain, and the probability mass flux absorbed for the first time at the critical surface gives the accumulation rate of fracture probability. Under the regularity conditions stated below, this rate equals the total outward probability flux across the absorbing boundary, while the Eyring–Kramers expression emerges as the small-noise, quasi-stationary approximation of this exact flux rate (Eyring 1935; Kramers 1940). In the present model, subcritical phase-field degrees of freedom are recoverable and may decrease locally during unloading, whereas event irreversibility is enforced through boundary absorption. Standard irreversible phase-field models that impose pointwise monotonicity constraints on the phase field (such as a nonnegative damage rate, $\dot{\phi}\geq 0$) therefore belong to a distinct constitutive class.

This study makes four contributions that together transform fracture probability from a snapshot diagnostic into a quantity generated by damage dynamics evolving in probability space:

1. Reflected–absorbed stochastic phase-field construction. Starting from the deterministic AT2 gradient flow, we formulate a reflected Langevin process on a bounded finite-element state space and designate the critical damage surface as an absorbing first-passage boundary, endowing the state space, drift mechanism, and boundary mechanism of probability evolution with clear mechanical counterparts. Because all stochastic analyses are conducted at the finite-element level, this construction can be implemented directly within standard finite-element codes.
2. Exact first-passage mass–flux identities. Fracture probability is identified with the probability mass absorbed at the critical surface: the loss of survival mass gives the cumulative fracture probability, the outward probability flux across the absorbing boundary gives its rate density, and the ratio of absorption flux to survival mass yields the exact effective hazard rate, forming a closed mass–flux balance.
3. Hierarchical treatment of uncertainty. Exogenous material, geometric, initial-state, and loading-history variables are collected in the exogenous input and held fixed within each conditional Fokker–Planck problem; stochastic loading histories are averaged over path space, whereas endogenous fluctuations enter solely through conditional diffusion, thereby placing distinct sources of randomness at their appropriate hierarchical levels of probability evolution.
4. Mechanical coupling and numerical verification. Survivor-conditioned damage provides a mean-stiffness closure with an explicit conditional-variance error identity, while first absorption yields the failure probability; seven numerical case studies demonstrate the complete stochastic–mechanical chain from the phase-field energy functional to engineering fracture probability.

Section 2 constructs the reduced deterministic AT2 gradient flow, introduces the effective reflected Langevin model, and derives its FP equation with an absorbing boundary, establishing the state space and evolution equation for probability evolution. Section 3 defines the first-passage fracture probability, derives the mass–flux and hazard identities, and examines the quasi-stationary, Kramers, and unloading regimes to characterize the rate structure of probability evolution. Section 4

distinguishes five categories of uncertainty sources and develops both configuration-resolved and mean-stiffness mechanical coupling schemes. Section 5 presents the seven numerical case studies, and Section 6 summarizes the main conclusions.

2 Stochastic phase-field model

2.1 Energy and reduced dynamics

The displacement field $\boldsymbol{u}$ determines the infinitesimal strain $\boldsymbol{\varepsilon}(\boldsymbol{u})$. The scalar phase field $\phi(x, t)$ ranges from zero for intact material to one for full degradation, apart from residual stiffness. The vector $\boldsymbol{\Phi}$ contains its N finite-element degrees of freedom.

For an elastic body occupying $\Omega \subset \mathrm{R}^d$, the AT2 potential with a tension–compression split (Miehe et al. 2010a) is

$$\begin{aligned}\Pi[\boldsymbol{u},\phi;t,\boldsymbol{\xi}] = \int_\Omega \left[g(\phi)\psi_0^+(\boldsymbol{\varepsilon}(\boldsymbol{u});\theta)+\psi_0^-(\boldsymbol{\varepsilon}(\boldsymbol{u});\theta)\right] \mathrm{d}x \\ + \int_\Omega \frac{G_c}{2}\left(\frac{\phi^2}{l}+l|\nabla\phi|^2\right) \mathrm{d}x - \boldsymbol{W}_{ext}[\boldsymbol{u};t,\boldsymbol{\xi}].\end{aligned} \tag{1}$$

Here ξ collects the exogenous inputs and θ denotes the material and geometric parameters. $G_c>0$ is the fracture toughness, $l>0$ the regularization length, $g(\phi)=(1-\phi)^2+\kappa$ the degradation function with $0<\kappa\ll 1$, ψ_0^+ and ψ_0^- the tensile and compressive strain-energy densities, and $\boldsymbol{W}_{ext}$ the external work. The corresponding viscous Allen–Cahn evolution is

$$\eta\dot{\phi} = -\frac{\delta\Pi}{\delta\phi} = 2(1-\phi)\psi_0^+ - \frac{G_c}{l}\phi + G_c l\Delta\phi, \eta>0. \tag{2}$$

Here $\eta > 0$ is the viscosity coefficient and Δ is the spatial Laplacian. The natural boundary condition is $\nabla\phi\cdot\boldsymbol{n}=0$ on $\partial\Omega$. At fixed loading and mechanical equilibrium, this flow dissipates energy.

The stochastic dynamics is constructed on the spatially discretized finite-element state space. A recoverable subcritical damage order parameter represents reversible microstructural evolution before fracture, and absorption at the critical boundary records the irreversible event.

For each discrete damage configuration Φ and prescribed load, solve quasi-static equilibrium with the mechanical boundary conditions:

$$\delta_{\boldsymbol{u}}\Pi[\boldsymbol{u}, \boldsymbol{\Phi}; t, \boldsymbol{\xi}]=0, \quad \boldsymbol{u}=\boldsymbol{u}_*(\boldsymbol{\Phi}, t; \boldsymbol{\xi}). \tag{3}$$

The stationarity condition holds for admissible displacement variations that satisfy the prescribed displacement constraints. Substituting this equilibrium into the total energy removes displacement from the stochastic state while retaining its dependence on damage. This defines the reduced potential

$$\Pi_N(\boldsymbol{\Phi}, t; \boldsymbol{\xi})=\Pi[\boldsymbol{u}_*(\boldsymbol{\Phi}, t; \boldsymbol{\xi}), \boldsymbol{\Phi}; t, \boldsymbol{\xi}]. \tag{4}$$

Assumption A0 requires the tracked stable equilibrium branch to be locally unique and smooth. If multiple branches are relevant, the stochastic state must include a branch label. With phase-field mass matrix $\boldsymbol{M}_\mathrm{h}$ and viscosity $\eta > 0$, finite-element discretization gives

$$\dot{\boldsymbol{\Phi}} = -\boldsymbol{M}\nabla_{\boldsymbol{\Phi}}\Pi_N, \quad \boldsymbol{M}=(\eta\boldsymbol{M}_\mathrm{h})^{-1}. \tag{5}$$

The constant mobility $\boldsymbol{M}$ is symmetric and positive definite. Retaining $\boldsymbol{M}_\mathrm{h}$ preserves the finite-element gradient metric and determines the corresponding noise covariance.

Each drift evaluation therefore solves mechanical equilibrium first and then evaluates the damage force at that equilibrium. Gradients of the reduced potential act on the damage coordinates $\boldsymbol{\Phi}$; the gradient penalty in Eq. (1) instead involves spatial derivatives of the phase field.

2.2 Reflected Langevin dynamics and fracture boundary

Unresolved mesoscopic fluctuations are represented by additive Gaussian noise on the finite-element damage vector. We assume that their correlation time is short relative to damage evolution, take the mobility to be constant, and use the Itô convention. State-dependent, colored or non-Gaussian fluctuations can be incorporated through generalized Langevin closures.

Even with ξ fixed, repeated realizations can differ because of these temporal fluctuations. Uncertainty in ξ describes variation between specimens, while dynamic forcing generates variability within each realization. The Langevin term supplies this additional conditional variability.

The ambient state space is $K=[0,1]^N$. A prescribed criterion $H(\boldsymbol{\Phi})\geq\phi_c$, with $0<\phi_c<1$, defines fracture. The intact domain is

$$O=\{\boldsymbol{\Phi}\in(0,1)^N: H(\boldsymbol{\Phi})<\phi_c\}. \tag{6}$$

For a local first-damage criterion, $H(\boldsymbol{\Phi})=\max_{1\leq i\leq N}\boldsymbol{\Phi}_i$; through-crack failure instead requires a crack-area, damaged-volume or connectivity criterion. The threshold must be calibrated with the mesh, regularization length and measurement definition. With nonnegative piecewise-linear basis functions, nodal reflection enforces the reconstructed field bounds.

For the maximum criterion, $O=[0,\phi_c)^N$: the faces $\boldsymbol{\Phi}_i=0$ reflect trajectories, and the faces $\boldsymbol{\Phi}_i=\phi_c$ absorb them. More generally, Γ_r and Γ_a denote the reflecting and absorbing boundary pieces. Conditions are imposed face by face and interpreted weakly at edges and corners (Skorokhod 1961; Tanaka 1979; Lions and Sznitman 1984; Saisho 1987; Ikeda and Watanabe 1989). Before absorption, the phase field satisfies

$$\mathrm{d}\boldsymbol{\Phi}_t=-\boldsymbol{M}\nabla\Pi_N(\boldsymbol{\Phi}_t,t;\boldsymbol{\xi})\mathrm{d}t+\sqrt{2\Theta_{eff}\boldsymbol{M}}\mathrm{d}\boldsymbol{W}_t-\sum_r \boldsymbol{M}\boldsymbol{n}_r(\boldsymbol{\Phi}_t)\mathrm{d}L_t^r. \tag{7}$$

Here $\boldsymbol{W}_t$ is an N-dimensional Wiener process, L_t^r increases only on reflecting face r, and $\boldsymbol{n}_r$ is its outward normal. The local-time term acts in the inward conormal direction, consistent with zero normal probability flux. At first contact with Γ_a, the trajectory is removed from the intact population and assigned to a cemetery state; it is never reinjected.

2.3 Effective noise intensity

The noise-amplitude matrix B is chosen to satisfy

$$\boldsymbol{B}\boldsymbol{B}^{\mathrm{T}}=2\Theta_{eff}\boldsymbol{M}. \tag{8}$$

The effective energy scale Θ_{eff} is a phenomenological parameter for mesoscopic fluctuations, calibrated from observations. At fixed loading with reflection on all boundaries, this closure gives a normalized Gibbs density proportional to $\exp(-\Pi_N/\Theta_{eff})$. This equilibrium consistency links fluctuations to dissipation (Callen and Welton 1951; Kubo 1966).

Before boundary handling, a Gaussian noise increment over a time step Δt has zero mean and covariance $2\Theta_{eff}\boldsymbol{M}\Delta t$. The finite-element mobility therefore determines both the magnitude and correlation of the coordinate increments; they need not be independent.

Absorption continually removes probability mass, making the transient surviving density and, under suitable conditions, the quasi-stationary distribution the relevant descriptions of the killed dynamics.

2.4 Fokker–Planck equation and probability flux

For a fixed exogenous realization ξ, let $p(\Phi, t|\xi)$ be the subprobability density of trajectories surviving before absorption at Γ_a. The failure criterion and boundary are fixed in time; loading enters through the drift. The probability current is

$$\boldsymbol{J}=p\boldsymbol{b}-\Theta_{eff}\boldsymbol{M}\nabla p=-\boldsymbol{M}\left(p\nabla\Pi_N+\Theta_{eff}\nabla p\right), \tag{9}$$

where $\boldsymbol{b}(\Phi,t;\boldsymbol{\xi})=-\boldsymbol{M}\nabla_{\Phi}\Pi_N(\Phi,t;\boldsymbol{\xi})$. The forward Fokker–Planck equation is the conservation law

$$\partial_t p=-\nabla\cdot\boldsymbol{J} \quad \text{in } O. \tag{10}$$

The reflecting and absorbing conditions are

$$\boldsymbol{J}\cdot\boldsymbol{n}_r=0 \quad \text{on } \Gamma_r; \qquad p=0 \quad \text{on } \Gamma_a. \tag{11}$$

For an initially intact ensemble, prescribe the nonnegative initial density as

$$p(\Phi, 0|\boldsymbol{\xi})=p_0(\Phi|\boldsymbol{\xi}), \qquad \int_O p_0\,\mathrm{d}\Phi=1. \tag{12}$$

The initial distribution is supported inside the intact domain and carries no mass on the absorbing boundary. Drift transports probability toward lower reduced energy, diffusion spreads it, and only absorption removes mass. These equations follow from Itô's formula and integration by parts; on nonsmooth boundaries they are understood weakly.

Here p retains the probability of survival: its integral decreases as paths are absorbed. Dividing by that integral gives the normalized distribution among survivors. At the absorbing boundary, the density vanishes while its gradient carries probability out of the intact domain.

PDEM/GDEE transports parameter uncertainty along deterministic conditional trajectories in response–parameter space (Li and Chen 2006, 2008, 2009; Zhang and Lv 2010). The present conditional FP equation includes a diffusion term generated by dynamic fluctuations and reduces to a pure transport equation in the zero-noise limit.

3 First-passage fracture probability

3.1 Survival mass, absorption flux and hazard

The first-passage time is

$$\tau_c=\inf\{t>0:H(\boldsymbol{\Phi}_t)\geq\phi_c\}, \tag{13}$$

with $\tau_c=+\infty$ if the boundary is never reached. Conditional on ξ, the survival probability and cumulative fracture probability are

$$S(t|\boldsymbol{\xi})=P_{intact}(t|\boldsymbol{\xi})=\int_O p(\Phi, t|\boldsymbol{\xi})\mathrm{d}\Phi, \tag{14}$$

$$P_f(t|\boldsymbol{\xi})=1-S(t|\boldsymbol{\xi}). \tag{15}$$

The initial density assigns total probability one to the intact population. Every first crossing removes a path permanently, so the missing mass is exactly the probability that fracture has already occurred. Subsequent unloading cannot return this mass. An instantaneous exceedance probability instead tests only the state at the observation time.

Integrating Eq. (10) over the intact domain converts its divergence into boundary flux. Reflection contributes zero, leaving only absorption. With positive, uniformly elliptic diffusion, a fixed boundary, an interior initial law and sufficiently regular coefficients and boundary traces, this gives

$$f_{\tau_c}(t|\boldsymbol{\xi})=\frac{\mathrm{d}P_f}{\mathrm{d}t}=-\frac{\mathrm{d}S}{\mathrm{d}t}=\int_{\Gamma_a}\boldsymbol{J}\cdot\boldsymbol{n}\mathrm{d}S\geq 0. \tag{16}$$

Thus fracture accumulates at the rate of outward absorption flux. For polyhedral domains, the balance holds weakly, with a classical normal-flux density under sufficient boundary regularity. For positive survival probability, the rate among surviving specimens is

$$k_{eff}(t|\boldsymbol{\xi})=\frac{f_{\tau_c}(t|\boldsymbol{\xi})}{S(t|\boldsymbol{\xi})}=\frac{\int_{\Gamma_a}\boldsymbol{J}\cdot\boldsymbol{n}\,\mathrm{d}S}{\int_O p\,\mathrm{d}\Phi}. \tag{17}$$

Over a short interval, the rate density multiplied by the interval length approximates the probability of a new fracture relative to the initial population. Hazard multiplied by the same interval length instead approximates that probability conditional on survival to the start of the interval.

The hazard is generally time dependent and still requires the transient density. With unit initial survival, its time integral gives

$$S(t|\boldsymbol{\xi})=\exp\left[-\int_0^t k_{eff}(s|\boldsymbol{\xi})\mathrm{d}s\right]. \tag{18}$$

The hazard is defined while survival is positive. This integrated relation holds for the full time-dependent hazard.

3.2 Quasi-stationary and Kramers approximations

At fixed loading, the density q_1 of the quasi-stationary distribution (QSD) and the principal decay rate k_1 satisfy

$$\mathrm{L}^* q_1=-k_1 q_1,\quad q_1\big|_{\Gamma_a}=0\quad \boldsymbol{J}[q_1]\cdot\boldsymbol{n}\big|_{\Gamma_r}=0,\quad \int_O q_1\,\mathrm{d}\Phi=1. \tag{19}$$

Here L* is the FP operator in Eq. (10). For a connected domain with uniformly elliptic diffusion and suitable regularity, the survivor-conditioned density converges to the QSD (Méléard and Villemonais 2012; Collet et al. 2013; Benaim et al. 2021). A small spectral gap can make convergence slow in a multiwell landscape. At fixed loading, after intrawell relaxation and when relaxation is much faster than escape,

$$p(\Phi,t|\boldsymbol{\xi})\approx S(t|\boldsymbol{\xi})q_1(\Phi;\boldsymbol{\xi});\qquad k_{eff}(t|\boldsymbol{\xi})\approx k_1(\boldsymbol{\xi}). \tag{20}$$

This factorization separates a nearly fixed distribution among survivors from its decreasing total mass. Flux and mass share the same amplitude, so their ratio approaches k_1. The principal eigenvalue applies beyond the small-noise regime introduced below. After this relaxation, the remaining first-fracture waiting time is approximately exponential.

An Eyring–Kramers reduction further requires a barrier large relative to the noise energy, a nondegenerate intact minimum a, a nondegenerate index-one saddle s, and separation of relaxation and escape times (Eyring 1935; Kramers 1940; Hänggi et al. 1990; Bovier et al. 2005; Freidlin and Wentzell 2012; Berglund 2013). For time-varying loads, a frozen-load approximation additionally requires loading to be slow relative to intrawell relaxation. Under these conditions,

$$k_1\approx A\exp\left[-\frac{V_{qp}}{\Theta_{eff}}\right], \tag{21}$$

where Vqp is the quasipotential from the intact well to the absorbing boundary. For fixed-load gradient escape through the controlling saddle, it equals the energy barrier $\Delta\Pi$ from the intact minimum to that saddle. For an interior saddle connecting two wells, the prefactor is

$$A=\frac{|\lambda_-(\boldsymbol{M}^{1/2}\boldsymbol{H}_s\boldsymbol{M}^{1/2})|}{2\pi}\sqrt{\frac{|\det\boldsymbol{H}_a|}{|\det\boldsymbol{H}_s|}}. \tag{22}$$

Here $\boldsymbol{H}_a=\nabla^2\Pi_N(a)$ and $\boldsymbol{H}_s=\nabla^2\Pi_N(s)$ are the Hessians at the minimum and saddle, and $\lambda-$ is the unique negative eigenvalue of $\boldsymbol{M}^{1/2}\boldsymbol{H}_s\boldsymbol{M}^{1/2}$. A saddle on or near the absorbing boundary, or absorption

at a nonstationary point, requires a different prefactor (Lelievre et al. 2025). Mobility anisotropy enters both drift and covariance; replacing consistent covariance by identical nodal noise changes the discrete model. Outside the Kramers regime, the flux-to-survival ratio remains the applicable hazard.

The transient FP solution provides the time-dependent hazard, the QSD eigenvalue describes its relaxed fixed-load limit, and Kramers theory estimates that eigenvalue from the local energy landscape. The accuracy of the Kramers approximation depends on separation of the relaxation, escape and loading time scales, the barrier-to-noise ratio and the saddle geometry. Section 5 compares these descriptions numerically.

3.3 Unloading and event irreversibility

Absorption makes cumulative fracture probability nondecreasing: an earlier first crossing remains a fracture event after unloading. Surviving trajectories may nevertheless move toward lower damage as the potential changes, reducing both their mean damage and the instantaneous hazard. Consequently, instantaneous threshold exceedance is not interchangeable with cumulative first passage.

Irreversible subcritical microcrack growth can be incorporated through history variables or complementarity constraints in the drift. Event irreversibility follows directly from boundary absorption in the open survival domain.

3.4 Computation in high dimensions

Direct grid solutions of the FP equation become impractical at realistic finite-element dimensions. Path simulation, rare-event sampling and splitting (Au and Beck 2001), reduced coordinates, or low-rank representations offer alternatives. A reduced coordinate may retain memory or state-dependent noise and therefore needs its own closure assessment. The same computational limits affect outer averaging and mechanical coupling. Case C7 examines joint identification of mobility and effective noise intensity using synthetic observations.

For each exogenous realization, computation starts from its initial density and loading history. Either evolve the surviving density or simulate reflected trajectories and remove each at its first boundary hit. Calculate survival and fracture probability before averaging over exogenous inputs. Where both quantities are available, agreement between lost survival mass and accumulated absorption flux checks the numerical probability balance.

4 Uncertainty and mechanical coupling

4.1 Conditional evolution and population averaging

Table 1 groups uncertainty by its entry into the model. S1–S4 describe uncertain material, geometry, loading, initial-state and model inputs; S5 is the dynamic noise remaining in each conditional process.

Table 1 Sources of uncertainty and their entry into the model

Category	Source	Examples	Model entry
S1	Material properties	Elastic modulus, toughness, length scale, residual stiffness	Parameters in reduced energy and mobility
S2	Geometry and defects	Notches, inclusions, initial microcracks, tolerances	Geometry parameters and a common reference domain
S3	Loading and environment	Load amplitude and frequency, impact, temperature, corrosion	Complete external history in the conditional drift

Category	Source	Examples	Model entry
S4	Initial states, observations and model choice	Initial density, parameter posterior, model choice	Outer averaging under an explicit probability model
S5	Unresolved dynamic fluctuations	Dislocation motion, grain-boundary slip, microcrack interactions	Conditional Langevin noise and FP diffusion

Collect all exogenous inputs in ξ and hold each realization fixed over its complete loading history. Their joint measure μ_{ext} includes a conditional measure on load paths and need not factor into independent inputs. Explicit probability models for initial-state, observation and model uncertainty enable population averaging; model bounds or sensitivity intervals describe sources represented without probability distributions.

For each ξ, solve the conditional FP problem and obtain S_ξ and P_f, ξ on its intact domain D_ξ. Each conditional absorbing surface remains fixed in time for the mass–flux identities used here.

The population fracture probability is

$$P_f^{pop}(t)=\int P_{f,\xi}(t)\mu_{ext}\mathrm{d}\boldsymbol{\xi}=1-\int S_\xi(t)\mu_{ext}\mathrm{d}\boldsymbol{\xi}. \tag{23}$$

The mixture subdensity is the corresponding outer average of the embedded conditional densities. Although evaluated at time t, it retains first-passage history because all earlier absorbed paths have been removed.

4.2 Population hazard and variance

For positive population survival, differentiating its outer average gives the survival-weighted hazard

$$k_{pop}(t)=\frac{\int k_\xi(t)S_\xi(t)\mu_{ext}\mathrm{d}\xi}{\int S_\xi(t)\mu_{ext}\mathrm{d}\xi}, \tag{24}$$

where k_ξ and S_ξ are the conditional hazard and survival. The arithmetic mean minus the population hazard equals $-\mathrm{Cov}(k_\xi, S_\xi)/E(S_\xi)$; its sign depends on that covariance. Let Y_t equal one if fracture has occurred by time t and zero otherwise. Let $q_t(\xi)$ denote the conditional fracture probability for that input realization. The law of total variance gives

$$\mathrm{Var}[Y_t]=\mathrm{Var}_{\mu_{ext}}\left[q_t(\boldsymbol{\xi})\right]+E_{\mu_{ext}}\left[q_t(\boldsymbol{\xi})\left(1-q_t(\boldsymbol{\xi})\right)\right]. \tag{25}$$

The first term measures variation among exogenous realizations, while the second is the average conditional Bernoulli variance. With a complete conditioning set ξ, the latter quantifies the contribution of S5. Comparing the magnitudes of these terms directly tracks the relative contributions of exogenous variability and endogenous dynamic fluctuations throughout loading.

4.3 Mechanical coupling and mean stiffness

Configuration-resolved coupling solves mechanical equilibrium for each damage state and uses its reduced-energy gradient in the drift. Under Assumption A0, the envelope theorem evaluates this gradient without differentiating the equilibrium displacement. This exact coupling uses repeated equilibrium solves, which can be accelerated by a controlled surrogate.

Write p_{mix} for the mixture subdensity and S_{pop} for its total surviving mass. For positive survival, normalize this density and compute the mean damage among intact specimens:

$$q_{mix}(\Phi,t)=\frac{p_{mix}(\Phi,\,t)}{S_{pop}(t)},\qquad S_{pop}(t)=\int_K p_{mix}\,(\Phi,\,t)\mathrm{d}\Phi. \tag{26}$$

$$\overline{\boldsymbol{\Phi}}(t)=E[\boldsymbol{\Phi}_t|\tau_c>t]=\int_K \Phi\, q_{mix}(\Phi,\,t)\mathrm{d}\Phi. \tag{27}$$

Dividing by survival makes q_{mix} integrate to one. The first moment of p_{mix}, without this division, equals survival multiplied by the mean damage of intact specimens. The normalized mean thus describes the specimens still available to carry load, while fracture probability records those already removed.

Mean damage and fracture probability are statistics derived from the governing density. Statistics covering fractured specimens additionally require a specified post-fracture response. Freezing each specimen at its first-passage configuration gives a stopped-process response; post-peak opening, contact or propagation requires additional dynamics.

At each spatial position x, reconstruct the scalar field $\phi(x;\Phi)$ from the nodal vector Φ using the finite-element basis. The exact mean degradation factor among survivors is

$$g_{eff}(x,t)=E\big[g\big(\phi(x,t)\big)|\tau_c>t\big]=\int_K g\left(\phi(x;\Phi)\right)q_{mix}(\Phi,\,t)\mathrm{d}\Phi. \tag{28}$$

For fixed material and loading parameters, or explicitly selected representative values, a cheaper intact-solid approximation substitutes the survivor mean into the degradation function and solves

$$g_{MF}(x,t)=g\left(\overline{\phi}(x,t)\right);\qquad -\nabla\cdot\big[g\big(\overline{\phi}\big)\sigma_0^{+}(\overline{\boldsymbol{u}})+\sigma_0^{-}(\overline{\boldsymbol{u}})\big]=\boldsymbol{b}_{ext}. \tag{29}$$

Here the mean phase field is reconstructed from the survivor-conditioned mean nodal vector using the common finite-element basis. The representative displacement is $\overline{\boldsymbol{u}}$, and the undegraded tensile and compressive stresses σ_0^{+} and σ_0^{-} are the strain derivatives of the corresponding energy densities, evaluated at this displacement. The body-force density is $\boldsymbol{b}_{ext}$; the prescribed displacement and traction conditions are retained.

For the quadratic AT2 degradation law, the local constitutive closure error satisfies

$$g_{eff}(x,\,t)-g\left(\overline{\phi}(x,\,t)\right)=Var(\phi(x,\,t)|\tau_c>t)\geq 0. \tag{30}$$

Equation (29) provides an efficient mean-field engineering closure in which the survivor mean damage determines tensile degradation. For the quadratic AT2 law, Eq. (30) shows that the local constitutive closure error between the exact survivor-averaged degradation factor and the factor evaluated at mean damage equals the survivor-conditioned variance.

5 Numerical studies

Seven cases test the framework, from analytical benchmarks to finite-element fracture and synthetic parameter identification (Table 2). Detailed parameter sweeps, convergence studies and repeatability checks are provided in the Supplementary Information (Online Resource 1). Fracture probabilities are computed from first-absorption times or surviving FP mass. Exogenous variables remain fixed throughout each specimen's loading history; endogenous fluctuations enter through conditional diffusion. Scalar examples write Θ for the effective noise intensity Θ_{eff}.

Table 2 Research questions for cases C1–C7

Case	Model	Purpose
C1	Reflected and absorbed drift-free diffusion	Analytical and path-wise mass–flux verification
C2	Quartic double well	QSD and Kramers validity
C3	Time-varying harmonic potential	First passage versus instantaneous exceedance during unloading
C4	Conditional FP ensemble	Outer averaging, hazard and variance
C5	AT2 rod with a weak zone	Consistent noise, first passage and mechanical coupling
C6	Notched plate with an inclusion	Coalesced cracks and competing paths
C7	Synthetic double-well inversion	Identification of mobility and noise intensity

Case C1: mass–flux and first-passage verification. Case C1 considers a one-dimensional stochastic diffusion model with a reflecting left boundary and an absorbing right boundary, using an analytical solution, a numerical Fokker–Planck solution, and Monte Carlo simulations to cross-validate the first-passage probability to the fracture threshold. The results confirm the consistency among the cumulative fracture probability, the loss of survival probability, and the time-integrated probability flux through the absorbing boundary.

A drift-free coordinate $q\in[0,L]$, with L=0.8, q_0=0.1 and $\mathrm{d}q=\sqrt{2D}\,\mathrm{d}\boldsymbol{W}$, reflects at q=0 and is absorbed at q=L. Rescaling by x=q/L and τ=Dt/L^2 removes the diffusivity. We compare an analytical cosine series, conservative finite volumes (N=400; Rannacher start-up, Crank–Nicolson; finest $\Delta\tau=2.5\times10^{-4}$) and 50,000 Brownian paths (finest $\Delta\tau=5\times10^{-4}$, with Brownian-bridge crossing correction). This uncoupled benchmark isolates the probability calculations. Fig. 1 compares the CDFs and numerical errors. The finest-grid maximum L^1 density error is 2.459×10^{-6}, the FP-to-analytical CDF Kolmogorov distance is 1.626×10^{-6}, and the discrepancy between lost survival mass and cumulative absorption flux is at most 4.711×10^{-11}. The Monte Carlo CDF error is 2.838×10^{-3}, with the analytical curve inside the Wilson 95% interval at every reporting time. Results for D=0.05, 0.1 and 0.2 collapse under the time rescaling. These checks confirm consistency among surviving mass, absorption flux and first-passage statistics; zero flux at the absorbing end or instantaneous exceedance probability would not reproduce this balance.

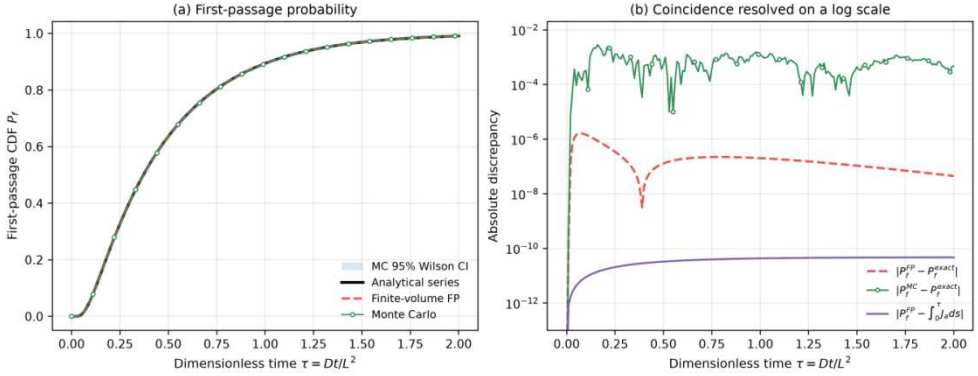


Fig. 1 C1 first-passage verification. (a) CDF $P_f(\tau)$ from the analytical series (black solid), finite volumes (red dashed) and Monte Carlo paths (green dots), with Wilson 95% confidence band (shaded). (b) FP and Monte Carlo errors and mass–flux residual on a logarithmic scale

Case C2: QSD and Kramers regimes. Case C2 considers a one-dimensional diffusion model in a double-well potential with reflecting and absorbing boundaries, verifying the formation of a quasi-

stationary distribution (QSD), the separation of intrawell relaxation and barrier-crossing escape timescales, and the agreement between the long-time hazard rate and the principal FP decay eigenvalue. Cross-comparisons of FP solutions, mean first-passage times, and Monte Carlo simulations assess the accuracy of the Eyring–Kramers formula under small-noise conditions and quantify its approximation error as the noise intensity increases.

We consider overdamped escape in the quartic potential $U(q)=\Delta\Pi[((q-0.5)^2/a^2)-1]^2$, with a=0.25, $\Delta\Pi$=1 and M=1, on $q\in(0,0.65)$, reflecting at q=0 and absorbing at q_c=0.65. The intact minimum is q_a=0.25, the saddle is q_s=0.5, and the barrier is $U(q_s)-U(q_a)$=1. The initial density is Gaussian near q_a with standard deviation 0.02; seven noise levels span $\Theta/\Delta\Pi$ = 0.04–0.20. Scharfetter–Gummel finite volumes use N=2048, with 50-digit Sturm bisection and inverse iteration to resolve eigenvalues as small as 10^{-10}. Fig. 2 compares the principal eigenvalue, inverse mean first-passage time (MFPT) from the backward equation, implicit-Euler transient hazard plateau and Kramers rate. The first three agree within 0.5% throughout and 0.001% at low noise; the plateau alone agrees with k_1 within a relative 10^{-9}. The conditional density approaches the QSD at the spectral-gap rate, while t_{relax}/t_{escape} rises from 3.2×10^{-12} to 1.6×10^{-3}, remaining well below unity. The low-noise slope of $\ln k_1$ against $\Delta\Pi/\Theta$ is −0.9989 (0.11% barrier error). At the three lowest noise levels, k_K/k_1=1.016, 1.020 and 1.027; at $\Theta/\Delta\Pi$=0.20, Kramers overestimates the rate by 8.6%. Moving the absorbing boundary changes the rate by less than 0.01% at low noise and up to about 4% at high noise. Thus, the principal eigenvalue gives the long-time rate after QSD formation, while Kramers becomes accurate in the small-noise regime with separated relaxation and escape times.

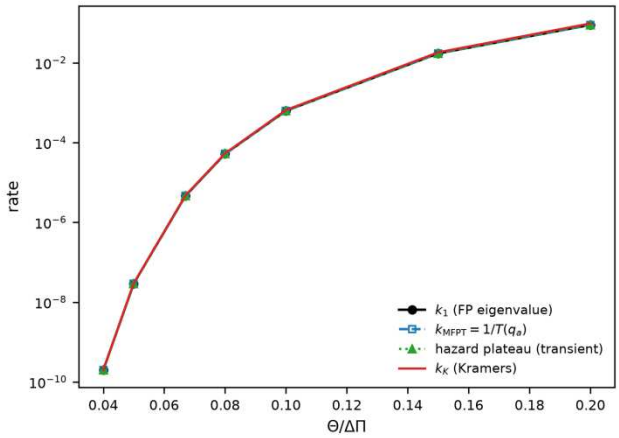


Fig. 2 C2 escape rates versus $\Theta/\Delta\Pi$ on a logarithmic scale: principal eigenvalue k_1, inverse MFPT, transient hazard plateau and Kramers rate

Case C3: loading and unloading. Case C3 compares cumulative first-passage and instantaneous threshold-exceedance probabilities under one-dimensional loading–unloading using absorbing-boundary FP solutions, a fully reflecting reference model, and Monte Carlo simulations. The results demonstrate that the mean state conditional on survival can recover during unloading, while cumulative fracture probability remains nondecreasing and consistent with the time-integrated absorbing flux. A one-dimensional coordinate evolves in $U(q,t)=\kappa[q-m(t)]^2/2$, with κ=10, M=1, Θ=0.01, q_0=0.1 and q_c=0.8. The load centre $m(t)$ rises smoothly (C^1) from 0.1 to 0.70 over $t\in[0,10]$, is held until t=15, returns to 0.1 over $t\in[15, 25]$, and remains there until t=35 (Fig. 3(a)). Model A reflects at q=0 and absorbs at $q=q_c$; the reversible reference, Model B, reflects at both ends of [0, 1]. Both use Scharfetter–Gummel fluxes and implicit Euler with $\Delta t=10^{-3}$, on 400 and 500 control

volumes, respectively. We also simulate 100,000 reflected Langevin paths using exact Ornstein–Uhlenbeck updates, half-step load freezing and Brownian-bridge crossing correction.

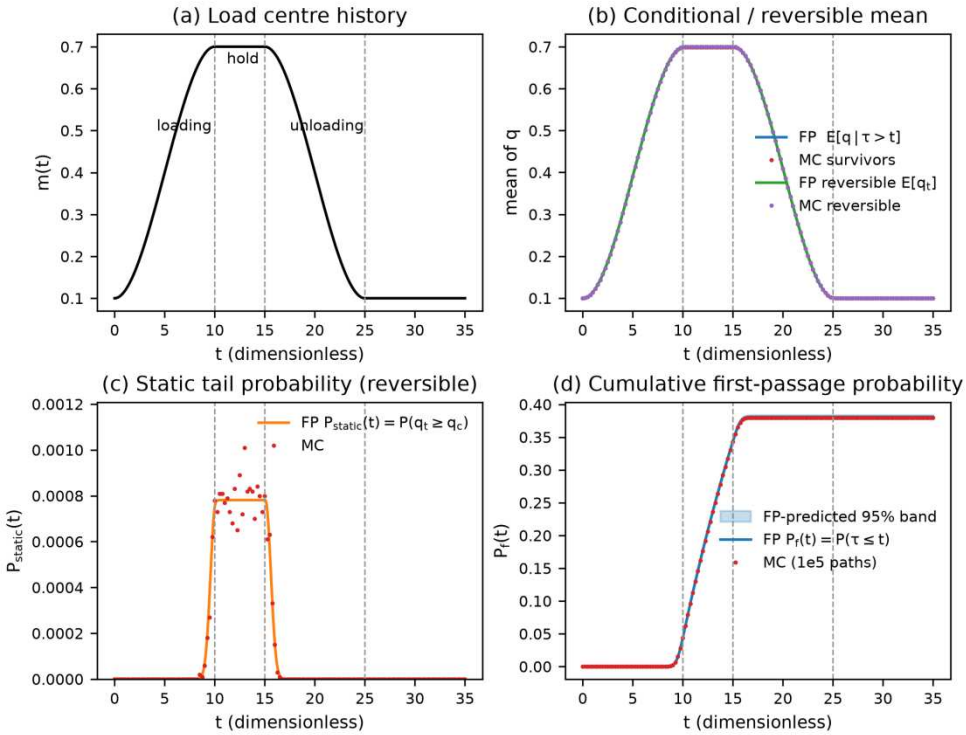


Fig. 3 C3 loading–unloading response. (a) Load-centre history; (b) survivor-conditional and reversible-process means; (c) instantaneous static tail probability; (d) cumulative first-passage probability $P_f(t)$ with path-simulation results

The FP fracture probabilities are 0.3438 at t=15 and 0.3809 at t=35, compared with path estimates of 0.3428 and 0.3796 (Fig. 3(d)). During unloading, the survivor-conditional mean falls from 0.6992 to 0.1001 (85.7%), alongside recovery of the reversible-process mean (Fig. 3(b)). Cumulative fracture probability remains monotone to round-off accuracy (minimum increment -8.9×10^{-16}). The instantaneous static tail probability is only 7.81×10^{-4} at t=15, about 440 times smaller than the fracture probability, and falls to 6.58×10^{-109} after unloading (Fig. 3(c)); the hazard similarly falls from 7.52×10^{-2} to 4.38×10^{-105}. The mass–flux discrepancy remains below 4.23×10^{-13}, and all Monte Carlo estimates lie within the FP 95% band over the active interval. Unloading therefore relaxes survivor damage and nearly suppresses new failures, but cannot reverse accumulated first-passage events.

Case C4: exogenous averaging and population hazard. Case C4 combines conditional FP solutions with outer parameter averaging to account for uncertainties in material properties, fracture thresholds, loading, and initial states, together with intrinsic noise. It computes population fracture probabilities, verifies the survival-weighted hazard relation, and decomposes failure uncertainty into external and intrinsic contributions using the law of total variance.

In the C3 problem, each specimen retains fixed $\xi=(\kappa,q_c,m_{max},q_0)$ throughout loading: κ is lognormal (mean 10, coefficient of variation 0.1); q_c is truncated normal (mean 0.8, standard deviation 0.02, range 0.72–0.88); m_{max} has mean 0.70, standard deviation 0.03 and truncation range 0.60–0.78; and q_0 follows mapped Beta(2,5) on 0.02–0.18. Conditional dynamics follow

$\mathrm{d}q=-\kappa[q-m(t)]\mathrm{d}t+\sqrt{2\Theta}\,\mathrm{d}\boldsymbol{W}$, with $\Theta=0.02$, reflection at $q=0$ and absorption at $q=q_c$. We use 1024 nested scrambled Sobol points, each with a conditional FP solution on 160 control volumes in $y=q/q_c\in[0,1]$ and $\Delta t=0.02$. The population fracture probability rises from 0.802333 to 0.820817 during unloading (t=15–25) and remains 0.820817 at $t=35$, with minimum increment zero. Conditional and population mass–flux residuals are at most 1.49×10^{-12} and 2.29×10^{-13}, respectively; refinement from 512 to 1024 Sobol points changes the final probability by 3.97×10^{-4}. In Fig. 4, the arithmetic mean hazard exceeds the survival-weighted population hazard. Their difference satisfies the hazard–survival covariance identity to 9.99×10^{-16}, while the total-variance identity closes to 1.46×10^{-16}. Sensitivities at $t=35$ rank as m_{max} ($\rho=0.811$), q_c (-0.541), κ (-0.075) and q_0 (0.002). High-hazard subpopulations are depleted more rapidly, producing a negative hazard–survival covariance, $\mathrm{Cov}(k_\xi,S_\xi)<0$. Equation (24) therefore explains why the unweighted arithmetic mean overestimates the population hazard in this example.

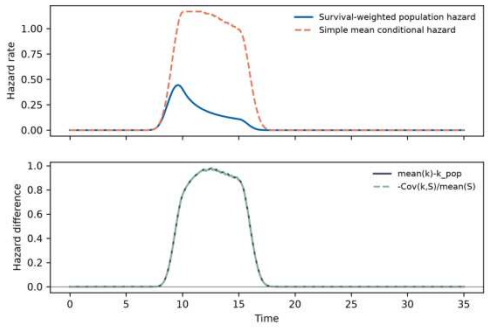


Fig. 4 C4 survival-weighted population hazard (blue solid) and arithmetic mean conditional hazard (orange dashed). The lower panel compares their difference with $-Cov(k_\xi,S_\xi)/E[S_\xi]$

Case C5: one-dimensional AT2 mechanics. Case C5 couples a one-dimensional AT2 phase-field model with quasi-static mechanics and introduces reflected Langevin noise consistent with the finite-element mass matrix, using Monte Carlo trajectories to calculate first-passage fracture probabilities under loading–unloading. The results demonstrate noise-induced fracture under deterministically subcritical loading, the coexistence of unloading recovery and irreversible cumulative fracture probability, and the equality between the mean-field closure error of quadratic degradation and the conditional damage variance.

A rod of length 10 mm and cross-section 1 mm^2 has $E=210$ GPa, $G_c=2.7$ N/mm and internal length l=0.25 mm, with a Gaussian weak zone reducing mid-length toughness by 10%. Displacement is condensed from quasi-static series-element equilibrium. Linear phase-field elements use AT2 energy, Gaussian increments consistent with the finite-element mass matrix and the mobility-based Langevin covariance, and conormal projection at $\phi=0$ in the mass-matrix metric. End displacement rises to 0.0430 mm over $t\in[0,10]$, is held for 2 time units, unloads over 10, and is held until $t=25$ (Fig. 5, top); the reference discretization is h/l=1/2, $\Delta t=0.0125$. Paths are absorbed when any node first reaches $\phi_c=0.95$. Five noise levels, $\bar{\Theta}=0$, 10^{-4}, 3×10^{-4}, 10^{-3} and 3×10^{-3}, use 2,000 paths per nonzero level. Deterministic runs on h/l=1/2, 1/4 and 1/6 never reach the threshold (peak reaction ≈531.9 N, relative span 0.00063%). At increasing nonzero noise levels, final fracture probabilities are 0.2305, 0.3540, 0.6155 and 0.9415 (Fig. 5, bottom); the middle panel compares survivor-conditional mean and rod-centre damage. The quadratic closure identity holds to 4.82×10^{-14}, the directional-derivative error is 6.92×10^{-11}, and the conormal-reflection KKT residual is below 7.66×10^{-13}. Final probabilities span 0.0025 across three time steps and 0.0275 (4.23% relative) across three stochastic grids, whose Wilson

intervals overlap at 400 paths per grid. These checks connect AT2 mechanics, consistent noise, reflection and first-passage absorption in a finite-element model.

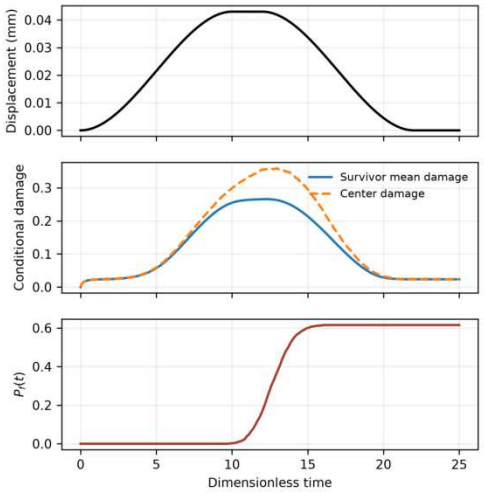


Fig. 5 C5 displacement history (top), survivor-conditional mean and rod-centre damage (middle), and cumulative first-passage probability $P_f(t)$ (bottom)

Case C6: two-dimensional competing crack paths. Case C6 uses independent stochastic phase-field simulations of a two-dimensional structure containing an inclusion to investigate competition between crack paths passing above and below it. It estimates path-selection probabilities, first-passage-time distributions, and cumulative fracture probabilities, while varying noise intensity and using mirror-paired comparisons to examine how stochastic perturbations influence crack branching and fracture timing.

A 50 *mm*×120 *mm* plate contains a left pre-notch and bonded circular inclusion (centre (36.5,60) mm, radius 10 mm, no internal phase-field freedom). Geometry and mesh are symmetric about y=60 mm under boundary displacements ±1.5t mm. Relaxed AT2 evolution uses l_0=0.8 mm, G_c=2280 J/m^2, E=6.24 GPa and v=0.28, with full stress degradation and a strain-energy spectral split. COMSOL Multiphysics integrates 39,676 matrix phase-field degrees of freedom using BDF1, relative tolerance 10^{-5} and maximum inner step 10^{-3} s. Every ΔT=0.01 s, a lumped-mass Gaussian increment is added and projected onto [0,1]; the viscosity coefficient is $d_a=10^{-3}$. Fracture occurs when the $\{\phi \geq 0.5\}$ zone first connects the pre-notch around the inclusion to x_{gate}=46.5 mm. Paths are classified as upper, lower, both or ambiguous. Prespecified weak, moderate and strong noise intensities are 1.5×10^{-13}, 1.5×10^{-12} and 1.5×10^{-11} m^2, with prespecified sampling and seeds. Moderate-noise sampling stops at N=64 when the Wilson 95% half-width falls below 0.12; 16 samples at each other level are used to assess sensitivity trends across noise levels. Deterministic run b00 remains short of the detection line through t=0.25 s, providing the right-censoring reference. Fig. 6 shows five crack histories. All 64 moderate-noise realizations fracture without censoring, with upper:lower =32:32, branch probabilities 0.500±0.119 (Wilson 95%), $\mathrm{CIF}_{\boldsymbol{upper}}(0.25)=\mathrm{CIF}_{lower}(0.25)=0.500$, and mean first-passage time 0.2021 s (median 0.202 s). Fig. 7 shows first-passage probability with a 95% bootstrap band and Aalen–Johansen cumulative incidences for the upper, lower and both branches. Weak- and strong-noise splits are 9:7 and 8:8. Three symmetry checks give machine-accurate mirrored trajectories, opposite branch labels and nearly identical first-passage times. Under this loading, timing is therefore largely controlled by the deterministic history, while noise selects near-degenerate branches without

detectable directional bias. The covariance functional obtained with lumped-mass sampling differs from its consistent-mass counterpart by about 4.1%.

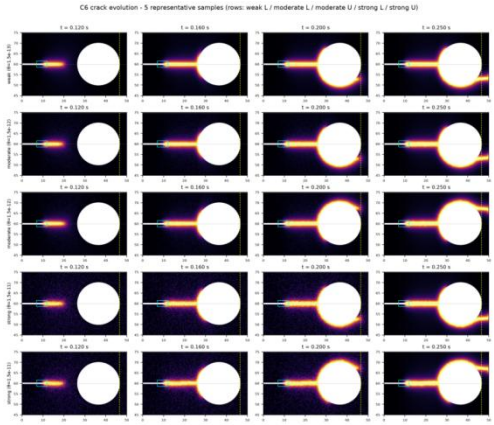


Fig. 6 C6 crack histories for five samples (rows) at t=0.12–0.25 s (columns). Dark to light indicates increasing damage; white circle: inclusion; cyan frame: pre-notch; yellow dotted line: detection line

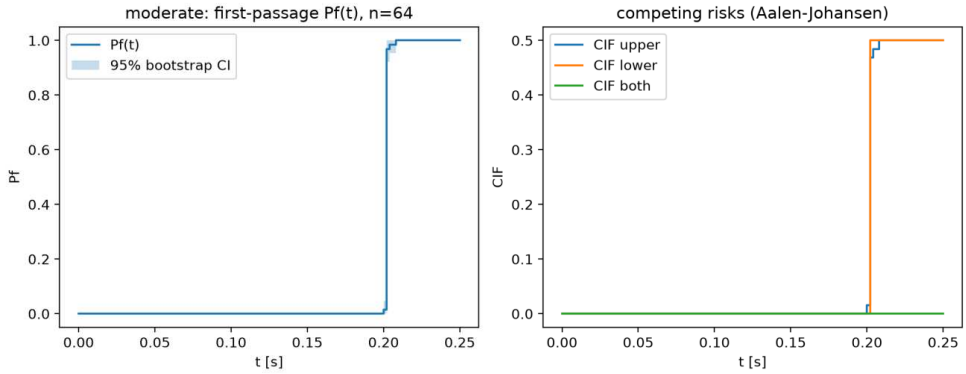


Fig. 7 C6 moderate-noise statistics. (a) First-passage probability $P_f(t)$ with 95% bootstrap confidence band; (b) Aalen–Johansen cumulative incidences of upper, lower and both branches

Case C7: synthetic identification of noise intensity and mobility. Case C7 uses synthetic data with known ground-truth parameters and prescribed energy landscapes to compare the identifiability of mobility and effective noise intensity from single-load first-passage data, multiple-load first-passage data, and additional intrawell relaxation observations. The results reveal strong parameter coupling with single-load data, substantially reduced uncertainty when multiple loads and relaxation autocorrelations are combined, and predictive validation using a held-out load.

In the C2 quartic potential, $\mathrm{d}\phi_t=-MU'(\phi_t;J)\,\mathrm{d}t+\sqrt{2M\Theta_{eff}}\,\mathrm{d}\boldsymbol{W}_t$ with $U=JV$, reflection at $\phi=0$ and absorption at $\phi_c=0.65$, three loads have barrier scales J=0.5, 0.65 and 0.8. The synthetic truth is $M^*=1$, $\Theta_{eff}^*=0.12$. Each load provides 500 first-passage paths with about 20% right censoring; 2,000 stationary trajectories in the lowest-barrier intact well provide a 64-lag relaxation autocorrelation. A Scharfetter–Gummel spectral expansion (N_q=256) supplies the first-passage density and survival likelihood for uncensored and censored observations, respectively. Posteriors are evaluated on a $(\log_{10}M,\log_{10}\Theta_{eff})$ grid for A (single-load first passage), B (three-load first passage) and C (B plus relaxation, using the full inter-lag covariance). Fig. 8 compares their marginals. For A, the correlation between $\log M$ and $\log\Theta_{eff}$ is −0.9948, and the 95% interval for M is [0.393,7.10]: the data mainly constrain $M\exp(-\Delta\Pi/\Theta_{eff})$. B narrows the intervals but retains a correlation of −0.9738. C gives

posterior modes M=0.989 and Θ_{eff}=0.1216 , with respective 95% intervals [0.9776,1.0099] and [0.1198,0.1223]. Interval width scales approximately as $N^{-1/2}$ (slope −0.489) and increases by 18% as censoring rises from 5% to 40%. The Kaplan–Meier 95% prediction band for replicated data has coverage 1.000 on hold-out loads. In this synthetic study, multi-barrier first-passage data and relaxation resolve the parameter trade-off: well covariance amplitude constrains noise intensity, while decay rate constrains mobility.

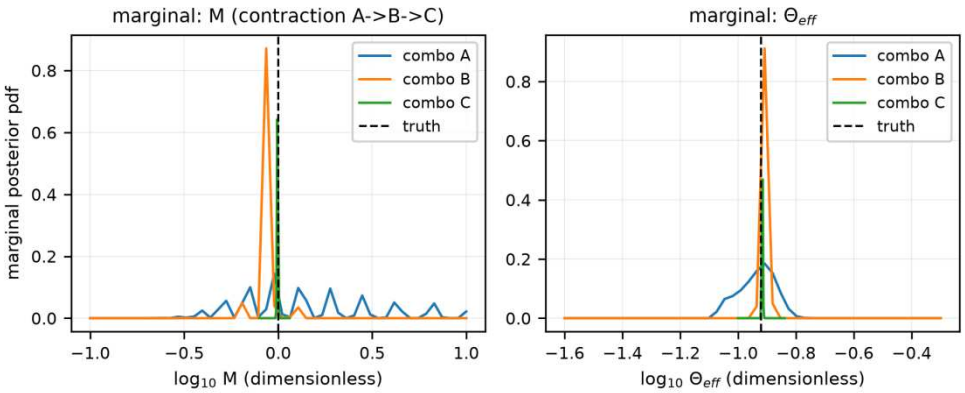


Fig. 8 C7 marginal posteriors of (a) M and (b) Θ_{eff} for A (single-load first passage), B (three-load first passage) and C (first passage plus relaxation). Dashed lines mark the synthetic truth

6 Conclusions

This study formulates fracture probability as a first-passage outcome of stochastic AT2 damage dynamics. Additive white Itô forcing with constant mobility represents effective mesoscopic fluctuations in the damage evolution. Reflection enforces state bounds, and absorption makes the first crossing of a critical surface irreversible. The killed FP equation then provides an exact mass–flux balance: fracture probability equals lost survival mass, its rate equals absorbing flux, and hazard is the flux-to-survival ratio. The Eyring–Kramers rate is a reduction valid under small noise, metastability and separated relaxation and escape times.

Exogenous uncertainty enters through an outer probability measure, while endogenous variability enters each conditional diffusion. This construction yields a survival-weighted population hazard and separates the two uncertainty contributions through total variance when the conditioning set is complete. Survivor-conditioned mean damage and fracture probability are derived from the same density. Under Assumption A0, configuration-resolved mechanics retains the full coupling, while mean-stiffness closure reduces the cost to one equilibrium solve, with a local degradation-factor error quantified by conditional variance.

Seven numerical cases test analytical mass–flux consistency, QSD and Kramers regimes, unloading, uncertainty mixtures, and one- and two-dimensional finite-element fracture. They show that survivor damage may relax during unloading while accumulated fracture probability remains irreversible. Competing-path simulations demonstrate noise-driven branch selection under symmetric loading. Synthetic identification further shows how multi-barrier first-passage observations and intact-state relaxation can jointly constrain effective noise intensity and mobility. Taken together, the numerical cases verify the framework's internal consistency and applicability across the studied loading and coupling conditions. The synthetic identification study establishes a direct methodological route toward calibration and validation with physical experiments.

Statements and Declarations

Author contributions

Z.Z. conceived the study, developed the methodology and the software, performed the formal analysis, prepared most of the figures, and wrote the original draft of the manuscript. P.G. conceived the study, supervised the work, and reviewed and edited the manuscript. C.D. developed the software, performed the formal analysis, and assisted with figure preparation. All authors reviewed and approved the final manuscript.

Funding

This work was supported by the National Natural Science Foundation of China (Grant No. 12102380).

Competing interests

The authors have no relevant financial or non-financial interests to disclose.

Data availability

Data and computational files supporting the numerical case studies are available from the corresponding author upon reasonable request.

Generative AI declaration

During preparation of this manuscript, the authors used Qoder and OpenAI Codex to improve readability and formatting. The authors subsequently reviewed and edited the content and take full responsibility for the manuscript.

References

Ambati M, Gerasimov T, De Lorenzis L (2015) A review on phase-field models of brittle fracture and a new fast hybrid formulation. Comput Mech 55:383–405. https://doi.org/10.1007/s00466-014-1109-y

Ambrosio L, Tortorelli VM (1990) Approximation of functionals depending on jumps by elliptic functionals via Γ-convergence. Commun Pure Appl Math 43:999–1036. https://doi.org/10.1002/cpa.3160430805

Au S-K, Beck JL (2001) Estimation of small failure probabilities in high dimensions by subset simulation. Probab Eng Mech 16:263–277. https://doi.org/10.1016/S0266-8920(01)00019-4

Bažant ZP, Pang S-D (2007) Activation energy based extreme value statistics and size effect in brittle and quasibrittle fracture. J Mech Phys Solids 55:91–131. https://doi.org/10.1016/j.jmps.2006.05.007

Benaim M, Champagnat N, Villemonais D (2021) Stochastic approximation of quasi-stationary distributions on compact spaces and applications. Ann Inst Henri Poincaré Probab Stat 57:726–739. https://doi.org/10.1214/20-AIHP1093

Berglund N (2013) Kramers' law: validity, derivations and generalisations. Markov Process Relat Fields 19:459–490

Bourdin B, Francfort GA, Marigo J-J (2000) Numerical experiments in revisited brittle fracture. J Mech Phys Solids 48:797–826. https://doi.org/10.1016/S0022-5096(99)00028-9

Bourdin B, Francfort GA, Marigo J-J (2008) The variational approach to fracture. J Elast 91:5–148. https://doi.org/10.1007/s10659-007-9107-3

Bovier A, Gayrard V, Klein M (2005) Metastability in reversible diffusion processes II: precise asymptotics for small eigenvalues. J Eur Math Soc 7:69–99

Callen HB, Welton TA (1951) Irreversibility and generalized noise. Phys Rev 83:34–40. https://doi.org/10.1103/PhysRev.83.34

Chandrasekhar S (1943) Stochastic problems in physics and astronomy. Rev Mod Phys 15:1–89. https://doi.org/10.1103/RevModPhys.15.1

Collet P, Martínez S, San Martín J (2013) Quasi-stationary distributions: Markov chains, diffusions and dynamical systems. Springer, Berlin. https://doi.org/10.1007/978-3-642-33131-2

COMSOL AB (2026) Theory for the phase field in solids interface. COMSOL Multiphysics 6.4 documentation. https://doc.comsol.com/6.4/doc/com.comsol.help.sme/sme_ug_theory.06.171.html. Accessed 4 August 2026

Eyring H (1935) The activated complex in chemical reactions. J Chem Phys 3:107–115

Francfort GA, Marigo J-J (1998) Revisiting brittle fracture as an energy minimization problem. J Mech Phys Solids 46:1319–1342. https://doi.org/10.1016/S0022-5096(98)00034-9

Freidlin MI, Wentzell AD (2012) Random perturbations of dynamical systems, 3rd edn. Springer, Berlin

Freudenthal AM (1968) Statistical approach to brittle fracture. In: Liebowitz H (ed) Fracture: an advanced treatise, vol II: mathematical fundamentals. Academic Press, New York, pp 591–619

Gardiner CW (2004) Handbook of stochastic methods for physics, chemistry and the natural sciences, 3rd edn. Springer, Berlin

Hänggi P, Talkner P, Borkovec M (1990) Reaction-rate theory: fifty years after Kramers. Rev Mod Phys 62:251–341. https://doi.org/10.1103/RevModPhys.62.251

Ikeda N, Watanabe S (1989) Stochastic differential equations and diffusion processes, 2nd edn. North-Holland, Amsterdam

Karma A, Kessler DA, Levine H (2001) Phase-field model of mode III dynamic fracture. Phys Rev Lett 87:045501. https://doi.org/10.1103/PhysRevLett.87.045501

Kramers HA (1940) Brownian motion in a field of force and the diffusion model of chemical reactions. Physica 7:284–304

Kubo R (1966) The fluctuation-dissipation theorem. Rep Prog Phys 29:255–284. https://doi.org/10.1088/0034-4885/29/1/306

Langevin P (1908) Sur la théorie du mouvement brownien. C R Acad Sci Paris 146:530–533

Lelievre T, Le Peutrec D, Nectoux B (2025) Eyring–Kramers exit rates for the overdamped Langevin dynamics: the case with saddle points on the boundary. J Ec Polytech Math 12:881–982. https://doi.org/10.5802/jep.303

Li J, Chen J-B (2006) The probability density evolution method for dynamic response analysis of non-linear stochastic structures. Int J Numer Methods Eng 65:882–903. https://doi.org/10.1002/nme.1479

Li J, Chen J-B (2008) The principle of preservation of probability and the generalized density evolution equation. Struct Saf 30:65–77. https://doi.org/10.1016/j.strusafe.2006.08.001

Li J, Chen J-B (2009) Stochastic dynamics of structures. Wiley, Singapore. https://doi.org/10.1002/9780470824269

Lions P-L, Sznitman A-S (1984) Stochastic differential equations with reflecting boundary conditions. Commun Pure Appl Math 37:511–537

Méléard S, Villemonais D (2012) Quasi-stationary distributions and population processes. Probab Surv 9:340–410. https://doi.org/10.1214/11-PS191

Miehe C, Hofacker M, Welschinger F (2010a) A phase field model for rate-independent crack propagation: robust algorithmic implementation based on operator splits. Comput Methods Appl Mech Eng 199:2765–2778. https://doi.org/10.1016/j.cma.2010.04.011

Miehe C, Welschinger F, Hofacker M (2010b) Thermodynamically consistent phase-field models of fracture: variational principles and multi-field FE implementations. Int J Numer Methods Eng 83:1273–1311. https://doi.org/10.1002/nme.2861

Rackwitz R (2001) Reliability analysis—a review and some perspectives. Struct Saf 23:365–395. https://doi.org/10.1016/S0167-4730(02)00009-7

Redner S (2001) A guide to first-passage processes. Cambridge University Press, Cambridge. https://doi.org/10.1017/CBO9780511606014

Risken H (1989) The Fokker–Planck equation: methods of solution and applications, 2nd edn. Springer, Berlin

Saisho Y (1987) Stochastic differential equations for multidimensional domain with reflecting boundary. Probab Theory Relat Fields 74:455–477

Skorokhod AV (1961) Stochastic equations for diffusion processes in a bounded region. Theory Probab Appl 6:264–274

Tanaka H (1979) Stochastic differential equations with reflecting boundary condition in convex regions. Hiroshima Math J 9:163–177

van Kampen NG (2007) Stochastic processes in physics and chemistry, 3rd edn. Elsevier, Amsterdam

Weibull W (1951) A statistical distribution function of wide applicability. J Appl Mech 18:293–297. https://doi.org/10.1115/1.4010337

Wu J-Y, Nguyen VP, Nguyen CT, Sutula D, Sinaie S, Bordas SPA (2020) Phase-field modeling of fracture. Adv Appl Mech 53:1–183. https://doi.org/10.1016/bs.aams.2019.08.001

Zhang W, Lv Y (2010) PDEM-based response analysis of nonlinear stochastic structures (in Chinese). J Vib Eng 23:447–454